Contents lists available at ScienceDirect

Food and Bioproducts Processing

journal homepage: www.elsevier.com/locate/fbp

Dehydration mechanisms in electrohydrodynamic drying of plant-based foods

Kamran Iranshahi[a,b], *Daniel I. Onwude*[a,c], *Alex Martynenko*[d], *Thijs Defraeye*[a,d,*]

[a] *Empa, Swiss Federal Laboratories for Materials Science and Technology, Laboratory for Biomimetic Membranes and Textiles, Lerchenfeldstrasse 5, CH-9014 St. Gallen, Switzerland*
[b] *Department of Environmental Systems Science, Swiss Federal Institute of Technology, ETH-Zurich, Zurich 8092, Switzerland*
[c] *Department of Agricultural and Food Engineering, Faculty of Engineering, University of Uyo, 52021, Uyo, Nigeria*
[d] *Department of Engineering, Dalhousie University, Faculty of Agriculture, Truro, Nova Scotia, Canada*

ARTICLE INFO

Article history:
Received 7 June 2021
Received in revised form 16 November 2021
Accepted 29 November 2021
Available online 3 December 2021

Keywords:
EHD
Mass transfer
Theoretical modeling
Diffusion
Electrocapillary flow
Thermocapillary flow

ABSTRACT

Electrohydrodynamic drying (EHDD) is an energy-efficient and non-thermal technique for dehydrating heat-sensitive biological materials, like fruits, vegetables, or medicinal plants. Although this method has been studied for more than three decades, still little is known about the relative contribution of the different dehydration mechanisms in EHDD. An accurate understanding of the impact of the different EHD-driven mass transfer processes inside the food and its surrounding air is essential for a targeted future optimization and successful upscaling of EHDD technology. Examples of these dehydration mechanisms are convective moisture removal, electroporation of the cell membrane, or electro-osmotic flow in the fruit. In this modeling study, we first identify possible dehydration mechanisms for mass transfer during the EHDD process of plant-based food materials. Using available theoretical models, we then estimate the relative contribution of each dehydration mechanism to the overall mass transfer during the constant rate period and rank them based on their contribution. We show that convective dehydration by ionic wind is the dominant dehydration mechanism, with a contribution of about 93% to the overall water flux for a capillary-porous material. Cell-membrane electroporation is the second important driving force that increases the contribution of the transmembrane water flow to about 6.5% of the total mass flux in fruit tissue. The contribution of all the other water transport mechanisms is only 0.5%. These insights provide a stepping stone towards developing a full physics-based model of the dehydration process by EHD, including the falling rate period.

* Corresponding author at: Empa, Swiss Federal Laboratories for Materials Science and Technology, Laboratory for Biomimetic Membranes and Textiles, Lerchenfeldstrasse 5, CH-9014 St. Gallen, Switzerland.
E-mail address: thijs.defraeye@empa.ch (T. Defraeye).
https://doi.org/10.1016/j.fbp.2021.11.009

1. Introduction

Drying is one of the oldest and most common techniques to preserve foods. It is also an essential unit operation in pharmaceutical, manufacturing, paper, polymer, and chemical industries. Drying involves evaporation of liquid water into the gaseous phase, usually via applying additional heat (Mujumdar and Devahastin, 2000). However, heat-based drying methods, such as hot-air drying or microwave drying, typically lead to losses of heat-sensitive active compounds in biological materials like fruits, vegetables, and medicinal plants (Lin et al., 1998; Gunasekaran, 1999; Jeyamkondan et al., 1999). Traditional drying methods for plant-based foods are usually energy-intensive, time-consuming, and lead to an extensive quality loss compared to the fresh product. In recent years, electrohydrodynamic drying (EHDD) has been considered as a promising non-thermal technology to avoid such quality damage in plant-based foods by drying fast but at a lower temperature (Singh et al., 2012; Bajgai et al., 2006). It is also a suitable technology for dewatering other materials in other areas such as ceramics and superconducting materials (Singh et al., 2012; Bajgai et al., 2006; Zhang et al., 2015). In addition, it is argued to be a more energy-efficient industrial unit operation compared to convective drying, although verification on an industrial scale was not yet done (Bajgai et al., 2006; Martynenko and Kudra, 2016; Iranshahi et al., 2020).

This promising technology relies on airflow generation due to a high voltage difference between two electrodes: an emitter that is connected to a high-voltage power supply and a collector that is usually grounded. The air around the emitter becomes locally ionized. The ions move from the emitter toward the grounded collector and transfer momentum to the neutral air molecules via collision. Thereby, airflow is generated, which is called ionic wind (Fig. 1a). This ionic wind accelerates the convective moisture removal from the material to be dried. Extensive research has been done on EHDD over the past two decades on a laboratory scale (Bajgai et al., 2006; Martynenko and Kudra, 2016; Defraeye and Martynenko, 2019; Leu et al., 2018). Progressive empirical (e.g. Martynenko et al. (2017)) and numerical models (e.g. Dolati et al. (2018), Defraeye and Martynenko (2018a)) have been developed. However, to date, researchers and industry have not yet been able to design a scaled-up robust industrial EHDD system. One of the reasons is that the efficiency and savings of an EHD dryer – in terms of drying time, energy, and costs – are not yet satisfactory for the industry. To prove exactly how much this technology could be superior, a better understanding of the underlying physics of the EHDD process is essential.

The drying efficiency is controlled by the driving forces of the water transport mechanisms inside the food material and the surrounding air. Lack of knowledge about these mechanisms in EHDD hinders further insight into the added values of this method compared to the other standard drying methods such as convective air drying. For instance, previous studies have reported a higher drying rate in EHDD compared to the equivalent forced convective drying, driven by mechanical ventilation (Martynenko et al., 2017; Bardy et al., 2015). However, not a lot of attention has been paid to why exactly such improvements in drying rate are obtained and what the relative contributions of each of the dehydration mechanisms are. Besides convective moisture removal, other physical mechanisms also contribute to moisture transport during the drying of plant-based foods, as driven by the electrical field and the ion flow (Martynenko et al., 2017). Hence, the reported increase in mass transfer rates by EHDD, compared to the forced convection, is likely attributed to the combination of several physical phenomena (Martynenko et al., 2017).

Several mechanisms of moisture transfer during EHD drying of food material are affected by the electric field and charged particles. Electric fields have a direct influence on charged particles such as free ions, dipoles, and polarizable molecules. Complex molecular structures such as membranes undergo structural rearrangements when they are exposed to a strong electric field (Zhang, 1991). This, in turn, changes resistance to water transport. To avoid this complexity, most of the previous theoretical works in EHD drying considered food as a simple porous media and all the water inside the material as bulk water, which transports by diffusion, without considering the impact of the electric field (Dolati et al., 2018; Defraeye and Martynenko, 2018a). They usually consider the impact of the electric field only on the generation of the airflow, i.e. ionic wind. To the best of our knowledge, there is no comprehensive study available that describes all the known dehydration mechanisms for EHD drying for plant-based materials and quantifies their relative contribution to the total mass flux during drying. Such a phenomenological understanding of the dominant dehydration mechanisms is essential for researchers and drying technologists to improve the EHDD process in terms of drying time and energy consumption to deliver superior quality products.

The main aim of the present work is to first identify various dehydration mechanisms for mass transfer during the EHDD process of plant-based food materials. Then, we quantify the relative contribution of each dehydration mechanism to the overall mass transfer under stationary drying conditions such as constant rate period using available theoretical models. Finally, we rank these transport mechanisms based on their relative contribution to the total dehydration rate under steady-state conditions. To do so, we composed a model of a single plant cell and a capillary to evaluate the water transport processes in three different regions of the cellular environment, intercellular environment or cell–air interface, and air. Based on the obtained results, a roadmap for EHD process optimization is suggested for future studies of EHD drying.

2. Process parameters and energy consumption in EHD drying

In this section, an overview of the typical process parameters in EHD drying is provided to describe the framework of the EHD drying process and our theoretical analysis.

2.1. *Electrical process parameters*

EHD drying relies on corona discharge in the gaseous medium and operates through applying a high voltage difference between two electrodes; emitter and collector. The typical electrical parameters that control the EHD drying process are voltage, type of current (direct or alternating), and polarity. The emitter is typically a set of metal wires with a diameter of several hundred micrometers or a needle with a tip radius of several hundred micrometers. The grounded collector is a metallic plate or mesh on which the drying material is placed (Fig. 1a) (Iranshahi et al., 2020; Defraeye and Martynenko, 2018a). The emitter-collector distance ranges from a few (e.g., 2–5 cm) to several tens of centimeters. Usually, the emitter is connected to a positive DC high voltage power supply, and the collector is grounded. The typical voltage difference between the emitter and collector is between 10 to 40 kV. The bulk electric field strength E_b [kV cm^{-1}] ranges from 1 to 10 kV cm^{-1}. Here, E_b is defined as the voltage difference divided by the distance between the electrodes. The local electric field intensity around the emitter is very high due to the large curvature of the emitter (i.e., sharp edges). It locally ionizes the air around the emitter. The minimum voltage required for corona discharge onset highly depends on the geometrical characteristics of the discharge and collector electrodes (curvature, emitter-collector gap, the spacing between the emitters) and the ambient conditions (humidity, temperature). This minimum voltage to initiate corona discharge can be calculated using Peek's formula (Peek, 1920). On the other hand, the maximum possible applied voltage is limited by spark-over or arcing between electrodes caused by the complete dielectric breakdown of the air. The occurrence of spark over is dependent on the geometrical parameters of electrodes and the ambient conditions.

2.2. Airflow and dehydration parameters

Although many studies consider ionic wind – hence convective water removal – as the principal driving force for EHDD (e.g. Martynenko et al. (2017), Lai and Sharma (2005)), the magnitude and direction of the airflow velocity are rarely measured experimentally. The measured average airspeed generated in EHD drying devices typically is between 0.1–10 m s^{-1} (Moreau and Touchard, 2008; Iranshahi and Mani, 2018; Monrolin et al., 2018). Ionic wind speed can also be estimated analytically based on current density (Robinson, 1961) or the bulk electric field strength E_b (Goodenough et al., 2007).

Due to the ionic wind, moisture is removed convectively from the material to be dried. Several parameters can accelerate the convective drying process. For instance, a higher air temperature, a lower relative humidity (RH) in the air, a higher ionic wind speed, and a better airflow distribution around the drying material lead to a higher convective dehydration rate. Besides convective dehydration, the presence of a strong electric field affects the drying rate by generating electrically-driven, so additional, moisture transport inside the material. In that case, the electrical process parameters (Section 2.1), not only indirectly affect the dehydration within the material by ionic airflow generation but also have a direct impact on water transport within the material.

2.3. Energy consumption

Energy consumption in EHDD involves the energy needed to produce the high voltage and the energy needed to maintain corona discharge. The energy to produce the high voltage is dependent on the high voltage power supply and AC/DC converter and their respective efficiencies. Although it is often measured in experimental EHDD studies, this value is highly equipment-dependent and changes significantly with the scale of the equipment. The energy use of the corona discharge process is therefore preferred as a scale-independent indicator of energy consumption. It only considers the power required for corona discharge P_E. The power required for the corona discharge P_E is typically less than 1 W (Singh et al., 2012; Monrolin et al., 2018), while the total power for the EHD process P_{tot} ranges from 1 to 50 W for a lab-scale EHD dryer (Martynenko and Zheng, 2016; Sumariyah et al., 2018). These values are highly dependent on the configuration of the electrodes (electrodes gap, the number of emitters and etc.), imposed polarity, and ambient conditions. For a constant voltage and electrode gap, increasing the number of emitters or the collector surface will increase the total corona ion current between emitter and collector and result in a higher P_E. It has recently been shown that utilizing an optimized collector surface can reduce P_E significantly for the same drying rate (Iranshahi et al., 2020).

The specific energy consumption (SEC, [MJ kg^{-1}]) is mostly used in EHDD because it also includes a quantity reflecting the drying rate of a product; thus, the amount of water evaporated. The SEC is defined as the consumed energy [MJ] per unit of water [kg] evaporated from a product (Defraeye and Martynenko, 2018b). Typical values for SEC based on the energy for corona discharge are 0.3–1.5 [MJ kg^{-1}] and based on total energy is 4–260 [MJ kg^{-1}] (Defraeye and Martynenko, 2018b). Compared to pure convective drying, in which airflow is generated by a fan, the specific energy consumption in EHDD was found to be at least 18 times less for the same drying rate in a lab-scale setup (Martynenko and Zheng, 2016). Nevertheless, extrapolating this difference in SEC to an up-scaled EHD dryer is debatable as there are different parameters such as HV converter efficiency, loading density and environmental conditions that will change in an industrial environment and up-scaled dryer.

3. Water transport mechanisms and quantification

3.1. General considerations

Tissues in plant-based foods like fruits and vegetables consist of an ensemble of cells with pores in between. The cells are composed of a cell wall, a cell membrane, and the protoplast (Fig. 1b) (Huang et al., 2012; Prawiranto et al., 2018). The protoplast contains a conductive jelly-like substance (i.e., cytoplasm) that surrounds other components in the cell, such as the vacuole. The cytoplasm is surrounded by a dielectric layer called the cell membrane (Tosteson, 1989). During drying, water is transported from the inside of this cellular material via the cell membrane to the cell wall and later into the intercellular air space. We identify in this study what the major water transport mechanisms for EHD drying in each region are. An overview of the considered dehydration mechanisms in different regions is shown in Fig. 2.

Inside the material to be dried, several processes are at play that affect water transport. These processes are indeed coupled. However, it is possible to perform kind of a sensitivity analysis study by comparing their impacts on the total water potential that is the driving force in the drying process. To this end, we analyze the EHD drying process by representing the water transport using mathematical models based on mass conservation equations. These conservation equations are expanded towards one variable, namely the capillary pressure (P_c) and are simplified further by taking into account some additional assumptions. Details about the applied simplifications and expansions are available in Section 2 of the supplementary material. As a result, the liquid water flux J_l [kg m^{-2} s^{-1}] and the diffusion flux for water vapor J_v [kg m^{-2} s^{-1}] are derived for porous media using Darcy's and Fick's laws, respectively (Whitaker, 1977; Datta, 2007; Defraeye and Verboven, 2017);

$$J_l = -\frac{k_l}{\mu_l}\rho_l \nabla P_c = -K_l \nabla P_c \tag{1}$$

$$J_v = -\rho_g D_{va,mat} \nabla x_v = -\rho_g D_{va,mat} \nabla \frac{\rho_v}{\rho_g} = -K_v \nabla P_c \tag{2}$$

where μ_l [kg m^{-1} s^{-1}] is the dynamic viscosity of the liquid, P_c [Pa] is the capillary pressure, and it is defined as the pressure difference between the liquid and gaseous phases inside a capillary. K_v [s] is the water vapor permeability due to the pressure gradient, K_l [s] is the liquid permeability of porous material for the liquid phase and k_l [m^2] is the hydraulic permeability of the porous media. $D_{va,mat}$ [m^2 s^{-1}] is the apparent diffusion coefficient for porous media, x_v is the water vapor concentration, ρ_l, ρ_v and ρ_g [kg m^{-3}] are the liquid, vapor, and gas densities, respectively. Note that instead of capillary pressure, also often the water potential ψ_i [Pa] is used, by which the total moisture flux through the material can be written as:

$$J_t = -K_t \nabla \psi = -(K_l + K_v)\nabla \psi \tag{3}$$

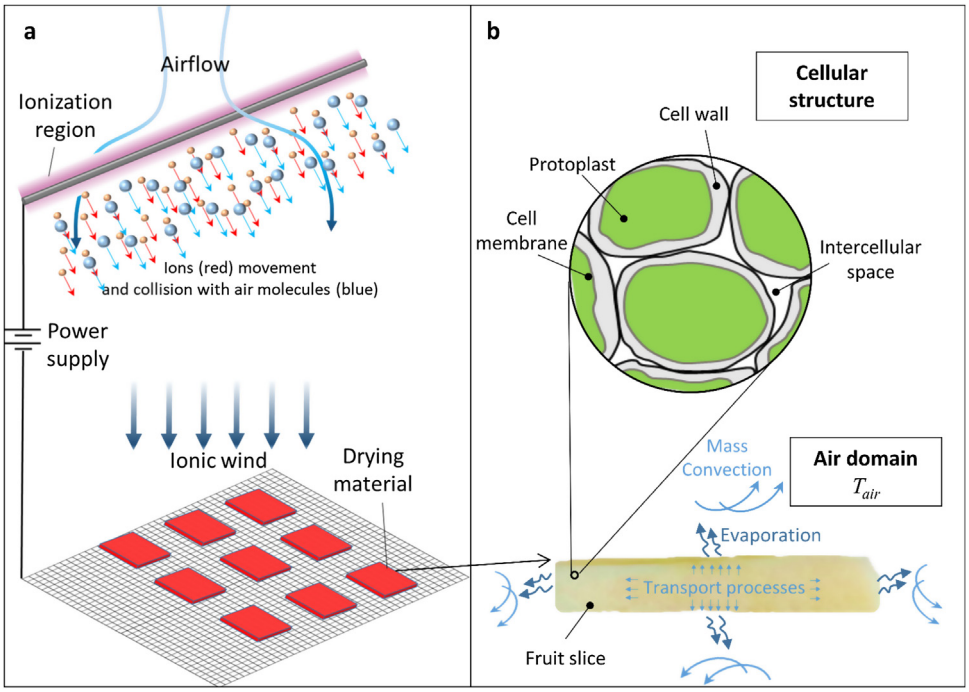

Fig. 1 – (a) Schematic of electrohydrodynamic drying setup with a wire-to-mesh configuration; (b) water transport together with the different cellular environment in which the water resides (figure not to scale).

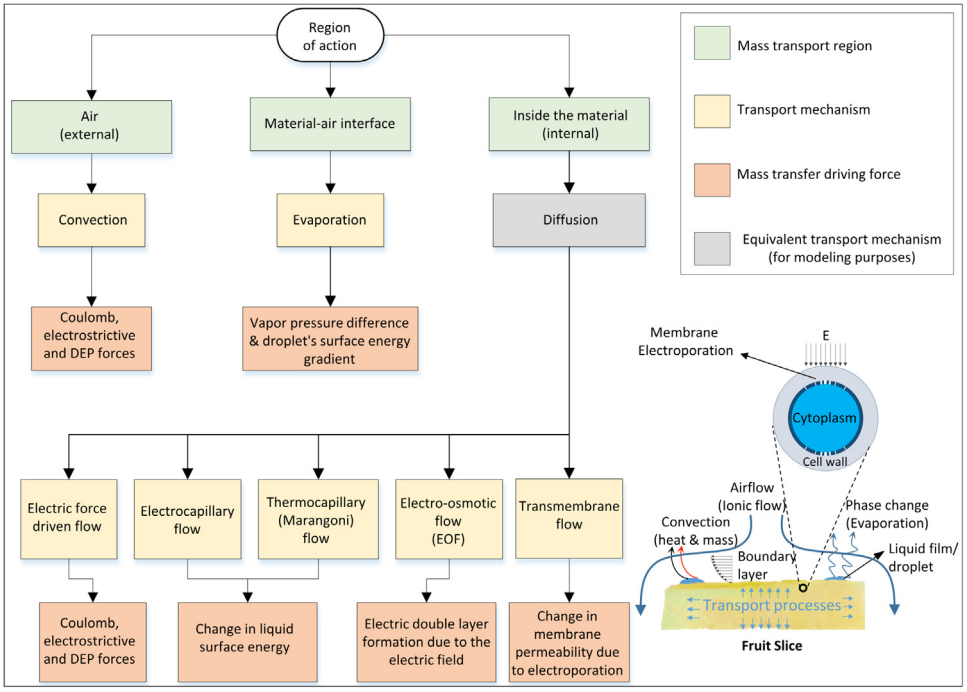

Fig. 2 – Water transport mechanisms classification based on the region of main action and origination together with a schematic illustration of transport mechanisms (not to scale).

K_t is the total permeability and ψ_i [Pa] is the water potential of component i of the porous media. The water potential difference (i.e., written in terms of capillary pressure) is the driving force for water transport. The resistance against water transport (i.e., opposite to the driving force) comes from the cellular structure, which includes the intercellular air space, the cell walls, and the cell membrane. These resistances are embedded in the water diffusivity and permeability coefficients. In the next sections, we evaluate how EHD affects the water transport process by lumping the impacts of the EHD-driven transport mechanisms into the driving forces or resistances. Such a methodology has been widely used in previous studies for modeling water transport at the cellular scale (see Huang et al. (2012), Prawiranto et al. (2018), Datta (2007), Aregawi et al. (2014)) and macroscale (see Diersch (2006), Liu et al. (2018), Di Fraia et al. (2018)).

It should be noted that the dehydration mechanisms are highly coupled and time-dependent with non-linear equations, especially during the falling rate period, which cannot be solved analytically and requires extensive numerical methods. The primary aim of this paper is to use a simple analytical formulation that could be understandable for a broad audi-

ence as this is the first step in modeling the dehydration mechanisms under EHDD. Therefore, we only considered the constant drying rate period, which is an important part of drying as it incorporates more than 50% of evaporated water in most biological materials (Mujumdar and Devahastin, 2000).

In this study, the effect of EHD on the drying process for apple fruit drying is quantified. The reason was that the required data to estimate the impact of each of the driving forces was available in a previous simulation-based study (Iranshahi et al., 2020). A rectangular slice of apple (10 mm × 5 mm) was considered as a drying material. We consider apple fruit placed on a wire-to-mesh configuration at operating voltages of 0 kV up to 30 kV (Fig. 1a). The theoretical models presented in the following sections were coded and implemented in MATLAB software. The script is available in the Supplementary materials.

3.2. *Convective moisture removal to the surroundings*

In this section, we estimate the contribution of convective dehydration to the total water transport process during EHDD. In electrohydrodynamic drying, the volumetric electrical force (F_E [N m^{-3}]) drives the ionic wind. The generated ionic wind enhances convection dehydration by reducing the mass transfer resistance of the boundary layer at the material–air interface. The dehydration process would stop when the vapor pressure at the material surface becomes equal to the partial vapor pressure of the drying air (Srikiatden and Roberts, 2007). This convective removal of water vapor is the only water removal mechanism in the air domain (external). It is usually argued to be the dominant driving force in the EHDD process (Martynenko et al., 2017) over other processes that EHD drying induces inside the material.

3.2.1. *Driving forces or resistances*

The difference in the vapor pressure at the surface of the material and the surrounding air is the driving force for convective moisture removal from the material–air interface (Martynenko et al., 2017; Alem-Rajabif and Lai, 2005). As mentioned, the presence of an airflow accelerates the process by lowering the resistance of the boundary layer to vapor removal. In electrohydrodynamic drying, the airflow is generated by the volumetric electrical force (F_E [N m^{-3}]). This body force quantifies how the electrostatic field and ion transport affect the airflow field. It appears in the momentum conservation equation (Eq. (4)) as a source term.

$$\rho_a \frac{\partial}{\partial t}(u) + \rho_a (u \cdot \nabla) u = -\nabla p + \mu_a \nabla^2 u + \rho_a g + F_E \tag{4}$$

$$F_E = \rho_c \vec{E} - \frac{1}{2}\varepsilon_0 |E|^2 \nabla \varepsilon + \frac{1}{2}\varepsilon_0 \nabla \left(|E|^2 \rho_a \frac{\partial \varepsilon}{\partial \rho_a} \right) \tag{5}$$

where ρ_a [kg m^{-3}] is the air density (1.20 kg m^{-3} at 20 °C), μ_a [kg m^{-1} s^{-1}] is the dynamic viscosity of air (1.81 × 10^{-5} kg m^{-1} s^{-1} at 20 °C), ε_0 electric permittivity of vacuum (8.854 × 10^{-12} C V^{-1} m^{-1}) and ε is the relative electric permittivity of the gaseous medium. Three electrically-induced forces act on a particle (i.e., molecules or ions), namely: the Coulomb force (first term in Eq. (5)), dielectrophoretic (DEP) force (second term in Eq. (5)) and, electrostrictive force (third term in Eq. (5)) (Iranshahi et al., 2020; Velev and Bhatt, 2006). The Coulomb force quantifies the net momentum gain due to the direct interaction between the electric field and the net surface charge of the charged particle. The DEP and electrostrictive forces result in the movement of a polarizable particle (not charged) in a non-uniform electric field due to the interaction of the particle's dipole and spatial gradient of the electric field and/or electric permittivity. A complete description of these electric forces is available in the supplementary material Section 3.

3.2.2. *Quantifying the impact of EHD-driven convection on the drying rate*

The dehydration rate by convection due to the ionic wind is quantified using Eqs. (4)–(10). To this end, the air velocity was used to calculate the convective mass transfer coefficient (h_m [m s^{-1}]), and h_m was used in Eq. (10) to calculate the mass transfer rate. In principle, the three contributions in Eq. (5) for ionic wind speed should be quantified. However, the typical values of these forces in EHDD show that the Coulomb force is larger than the other two forces by 2–3 orders of magnitude. The electrostrictive force is only significant if there are large gradients in the density of air, for example, when high-temperature gradients appear. The dielectrophoretic force plays a role if a strong alternating electric field is applied with a high frequency (Shrimpton, 2009). Accordingly, in single-phase, quasi isothermal air with DC voltage, these two forces are typically negligible, and only Coulomb force drives the airflow. The average generated airspeed due to the Coulomb force (Eq. (4)) can be estimated based on (Robinson, 1961):

$$\overline{u}_e = \sqrt{\frac{\varepsilon_0}{\rho_a}} E \tag{6}$$

The quantified values are shown in Fig. 3. The average values are calculated over a defined region of interest (ROI) around the sample. For this purpose, a rectangle with a width of 10 sample length (L_s) and a length of 5L_s around the sample is considered. The proper correlation of the convective mass transfer coefficient (CMTC) h_m [m s^{-1}] that results from the ionic airflow field is estimated by the following formula (Cengel, 2014; Plumb, 2000):

$$h_m = \frac{D_{va} \times Sh_L}{L_s} = \frac{0.332 \times D_{va} (Sc)^{\frac{1}{3}} (Re)^{\frac{1}{2}}}{L_s} \tag{7}$$

where Sh_L is the Sherwood number, L_s is the characteristic length of the sample, which in our case is considered as 0.01 m, D_{va} is the mass diffusivity of water vapor to air (2.42 × 10^{-7} m^2 s^{-1} at 20 °C), *Sc* and *Re* are the Schmidt and Reynolds numbers, respectively. In order to calculate h_m two dimensionless numbers, namely Schmidt (*Sc*) and Reynolds (*Re*) numbers should be calculated as follows:

$$Sc = \frac{\nu}{D_{va}} \tag{8}$$

$$Re = \frac{\overline{u}_e L_s}{\nu} \tag{9}$$

where ν is the kinematic viscosity of air (1.5 × 10^{-5} m^2 s^{-1} at 20 °C). Having these numbers, h_m can be calculated from Eq. (7) Cengel (2014). With h_m, the steady-state water removal rate (i.e., the convective mass flux from the surface) can then be calculated as:

$$J_c = -D_{va} \times Sh_L \frac{(C_w - C_{w\infty})}{L_s} = -h_m (C_w - C_{w\infty}) \tag{10}$$

where C_w and $C_{w\infty}$ [kg m^{-3}] are the water vapor concentration of the material surface and ambient air, respectively.

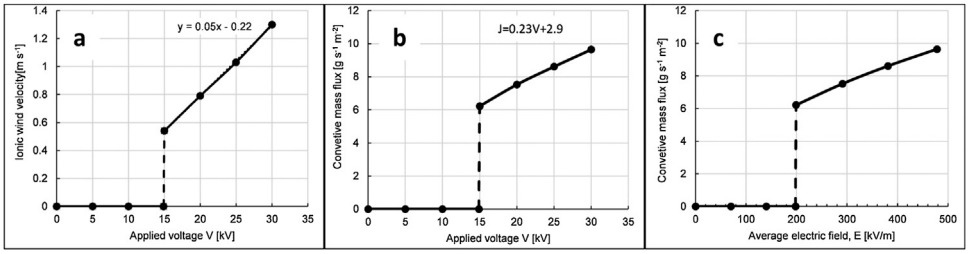

Fig. 3 – Quantified values for convective dehydration; (a) average airflow (ionic wind) velocity by applying different voltages, (b) the convective mass flux in different voltages, and (c) the convective mass flux with respect to the average electric field in the region of interest.

Assuming that both the air and water vapor are ideal gases, the calculated values were $C_w = 0.0173$ and $C_w\infty = 0.0052$ [kg m^{-3}] based on the ideal gas law.

The results are shown in Fig. 3. In EHD, corona discharge starts when the applied voltage and the electric field are sufficiently large to induce the local breakdown of the air. The voltage at the wire is increased until the electric field in the proximity of the wire becomes sufficiently large to induce the local breakdown of the air. In the configuration considered in this study, corona discharge happens for voltages higher than 10 kV, and before that, the ionic wind velocity is zero (Fig. 3a). Increasing the voltage beyond the critical voltage up to 30 kV increases the ionic wind velocity and the convective mass flux quasilinearly.

3.3. *Evaporation at the material–air interface*

In this section, the evaporation of surface water at the material–air interface in the context of electrohydrodynamic drying will be investigated. This water can be present as a liquid water film or water droplets. Based on the size of the droplets, different forces affect the evaporation rate (Zang et al., 2019). For drying of foods, the water films and droplets are of macroscopic size, so intermolecular forces that play a role in nano capillaries are not relevant here. In a sessile droplet, water molecules evaporate if excess energy (i.e., latent heat of evaporation) is available so the molecule can overcome the internal cohesive forces. Moreover, they can only escape the droplet if there is a driving force for moisture transport, i.e., if the surrounding air is not fully saturated with water vapor (Schönfeld, 2008).

3.3.1. *Driving forces or resistances*

A vapor pressure difference between the surface of the droplet and the surrounding environment drives the evaporation process. The energy required to induce evaporation, the enthalpy of vaporization, has to be supplied to the system to complete the liquid–vapor phase transformation (Garai, 2009). This energy is usually taken from the product to be dried and the surrounding air. This leads to a temperature decrease down to the wet-bulb temperature in the case of purely convective transfer. The surface energy plays an important role in the magnitude of the required enthalpy of vaporization (see Eq. (11)) (Garai, 2009; Jiang et al., 2016; Nikzad et al., 2017).

$$\Delta H_V = \Delta U_V + \Delta w_V = \gamma_{LV} A_{drop} + P\,(V_V - V_L) \tag{11}$$

where ΔH_V [kJ mol^{-1}] is the enthalpy of vaporization, ΔU_V [kJ mol^{-1}] shows the variation of the internal energy of the system, Δw_V [kJ mol^{-1}] is the external work of the expansion from liquid to gas, γ_{LV} [mN m^{-1}] is the liquid–vapor surface tension, A_{drop} [m^2] is the surface area of the drop or film, P [Pa] is the pressure, V_V is the volume of the vapor, and V_L is the volume of the liquid.

Several factors, including temperature and the electric field, have direct impacts on the droplet's surface energy needed to evaporate the droplet (Nikzad et al., 2017; Vancauwenberghe et al., 2013). The electric field tends to realign polar molecules such as water. Consequently, the electric field can improve the evaporation flux by modifying the surface energy and contact angle of the droplet (Vancauwenberghe et al., 2013). The change of the contact angle is called the electrowetting effect. This effect implies that due to the electric field, the contact angle decreases, by which the droplet spreads more and surface wetting increases. As such, the evaporation of these droplets or films can differ for electrohydrodynamic drying compared to normal convective drying.

3.3.2. *Quantifying the impact on the drying rate*

Evaporation is only assumed to occur at the surface, implying that moisture transport occurs via the liquid phase and not by water vapor. This assumption is less accurate during the final stages of drying, so at very low moisture contents. The contact angle variation under electric field can be calculated from Digilov (2000):

$$\cos(\theta_e) = \cos(\theta_0) + \frac{C_{sl}(\varphi_{SL} - \varphi^0_{SL})^2}{2\gamma_{SL}} \tag{12}$$

In the above equation, θ_e is the contact angle under the electric field, θ_0 is the contact angle without the field (i.e., typically between 55° to 80° for water on a food material (Ramírez et al., 2012; Choi et al., 2002)), and γ_{SL} (=29.2 mN m^{-1} for water on apple (Sapper et al., 2019)) is the interfacial tension of the solid-liquid phase at the zero potential φ^0_{SL}, and φ_{SL} [V] is the potential applied to the interface of the three-phase system obtained from simulation results available in Iranshahi et al. (2020). C_{sl} [F] is the capacitance of the interface $C_{sl} = \varepsilon_m / d_{sample}$ where ε_m [F m^{-1}] corresponding to the electric permittivity of the material in contact with the liquid drop ($\varepsilon_m = 80\varepsilon_0$ for apple tissue), and d_{sample} [m] is the material thickness. The variation of the liquid-vapor surface tension (γ_{LV}) can be estimated by Young's formula (Zang et al., 2019):

$$\gamma_{LV} = \frac{\gamma_{SV} - \gamma_{SL}}{\cos(\theta_e)} \tag{13}$$

In the above equation, γ_{SV} (=65.3 mN m^{-1} for apple fruit) is solid-vapor surface tension. The variation of the surface energy and contact angle with respect to different applied voltages at the emitter electrode are shown in Fig. 4a and b.

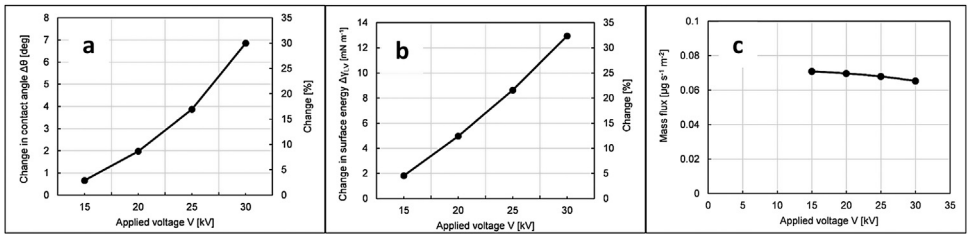

Fig. 4 – Quantified values for the evaporation at the material–air interface; (a) variation of the contact angle with respect to different applied voltages at the emitter electrode, (b) variation of the liquid-vapor surface tension with respect to different applied voltages at the emitter, and (c) the mass flux with respect to the applied voltages.

Based on our simulation results (see Defraeye and Martynenko (2018a)), increasing the emitter's voltage up to 30 kV increases the electric potential of the fruit surface up to 320 V. Increasing the voltage changes the surface tension and contact angle exponentially. However, the variations are small for the range of voltages investigated in this study. Based on our calculations, the water surface energy and contact angle on the fruit surface (θ_e) for such a voltage do not change more than 10° for the applied voltages up to 30 kV.

In the literature, it is usually assumed that the diffusion of molecules controls the total evaporation flux of a droplet from the liquid–gas interface to the surrounding air. Hence it is generally described by Fick's law (Vancauwenberghe et al., 2013; Semenov et al., 2011):

$$J_{eva} = -2\pi R_{drop} D f(\theta_e)(C_s - C_\infty) \tag{14}$$

where J_{eva} is the evaporation flux [kg m^{-2} s^{-1}], R_{drop} is the initial wetting radius [m], D is the diffusion coefficient [m^2 s^{-1}], C_s is the saturated concentration of vapor at the drop interface [kg m^{-3}], and C_∞ is the concentration of vapor in the air [kg m^{-3}]. $f(\theta)$ is a function of the contact angle derived by Picknett and Bexon (Semenov et al., 2011; Picknett and Bexon, 1977):

$$f(\theta_e) = \begin{cases} \dfrac{0.6366\,\theta_e + 0.09591\,\theta_e^2 - 0.06144\,\theta_e^3}{\sin(\theta_e)} & \text{when } \theta_e < 10^\circ \\ \dfrac{0.00008957 + 0.6333\theta_e + 0.116\theta_e^2 - 0.08878\theta_e^3 + 0.01033\theta_e^4}{sin(\theta_e)} & \text{when } \theta_e \geq 10^\circ \end{cases} \tag{15}$$

The results of the quantifications for a drop with a radius of 500 μm are shown in Fig. 4. Higher voltages up to 30 kV do not change the mass flux and evaporation significantly. This is due to the small variation in surface energy, as discussed in previous paragraphs. A slight variation in the surface energy means a small change in contact angle (θ_e), hence $f(\theta_e)$ and consequently J_{eva}. In other words, under EHD, the evaporation at the material–air interface does not change significantly because the change in the surface energy, and in turn enthalpy of evaporation, is too small.

3.4. *Electric force-driven flow*

This section quantifies how electrical forces affect vapor transport inside porous media such as fruit tissue during EHDD. Water exists in the vapor phase inside fruit tissue capillaries since we assume that no condensation occurs (Prawiranto et al., 2018). The transport process of the air and water vapor mixture in a porous material consists of advection and diffusion (Diersch, 2006). Electric forces can affect this transport process by inducing the electrical body force F_E. Under an electric field, different components inside the fruit tissue, such as cell walls and capillary surfaces, obtain electric charges on their surfaces (Li, 2004). The charge on these surfaces, in turn, results in an unbalanced charge distribution, which leads to the electric force-driven flows (EFDF) in liquid or vapor phases (Li, 2004). In Section 3.2, we have already introduced the electrical force F_E and its three components that act on an air molecule, namely: the Coulomb force, dielectrophoretic (DEP) force and, electrostrictive force.

3.4.1. *Driving forces or resistances*

Neglecting gravity, the water potential gradient resulting from the pressure gradient and water molecule concentration gradient is the driving force of the advective–diffusive process. During EHDD, isobaric conditions exist, and the pressure gradient is zero. Nevertheless, the volumetric electric force F_E [N m^{-3}] induces a pressure gradient, hence a water potential gradient.

3.4.2. *Quantifying the impact on the drying rate*

The formulation of F_E was already mentioned in Section 3.2 (Eqs. (4) and (5)) for properties related to air. The same relations are applicable here but for water vapor properties. We use a subscript $F_{E,v}$ to differentiate the electric forces inside and outside the material. $F_{E,v}$ consists of Coulomb, DEP and electrostrictive forces. The temperature variation inside the material during EHDD is negligible, so the electrostrictive force is considered zero. The DEP force, F_{DEP}, is dependent on the gradient of the field squared, ∇E^2 and the particle radius cubed (i.e., proportional to particle volume) (Velev and Bhatt, 2006; Washizu et al., 1994):

$$F_{DEP} = 2\pi\varepsilon a_p^3 \nabla E^2 Re\,|K| \tag{16}$$

where K is Clausius–Mossotti function (see Velev and Bhatt (2006), Washizu et al. (1994)), a_p is the particle radius, and ε is electric permittivity of the medium. Based on this formulation, DEP force scales with particle radius cubed, and it can be neglected for small particles especially when the particle is in molecular size (Washizu et al., 1994). For calculating the Coulomb force $F_{C,EFDF} = \rho_{e,EFDF}\vec{E}$, we estimated the average space charge density $\rho_{e,EFDF}$ based on average $\vec{E}$ inside the material. The latter is obtained from our simulation results. The forces was divided by the characteristic area of the material A_s to translate this force into the pressure form $P_{c,EFDF}$ [Pa].

$$P_{c,EFDF} = F_{C,EFDF}/A_s \tag{17}$$

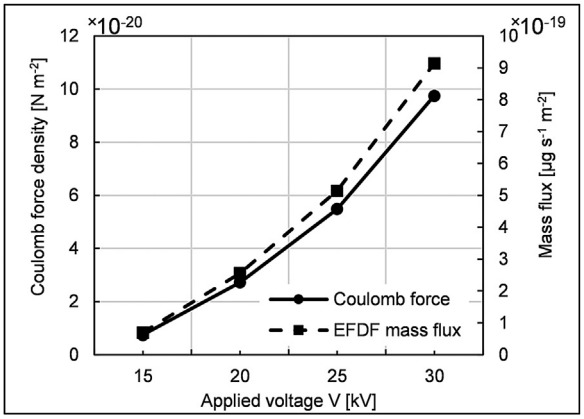

Fig. 5 – Quantified values for the electrical force-driven flow (EFDF) inside the material; variation of Coulomb force and EFDF mass flux inside the material vs. applied voltages at the emitter electrode.

Neglecting the gravity, the vapor flux in porous media can be written as follows (Diersch, 2006);

$$J_{v,EFDF} = -K_{v,EFDF}\nabla\psi_{c,EFDF} = -\frac{k_v}{\mu_{ma}}\rho_v\nabla P_{c,EFDF} \tag{18}$$

where μ_{ma} [kg m^{-1} s^{-1}] is the dynamic viscosity of moist air (18.13 × 10^{-6} kg m^{-1} s^{-1} at 20 °C) and ρ_v is the density of water vapor (0.017 kg m^{-3} at 20 °C). $k_v \cong 10^{-13}$ m^2 (Feng et al., 2004) is the effective gas permeability of the porous media which contains the impact of the molecular, or Knudsen, diffusion through the Klinkenberg coefficient, b:

$$k = k_0\left(1 + \frac{b}{P_g}\right) \tag{19}$$

where P_g is the gas pressure and $k_0 \cong 10^{-13}$ m^2 (Feng et al., 2004) is intrinsic hydraulic permeability.

To compare the results with natural gas diffusion (i.e., diffusion without EHD effect), we considered a single capillary with saturated vapor concentration at the one end and employed diffusion flux due to vapor concentration:

$$J_v = -\rho_g D_{va,mat}\nabla\frac{\rho_v}{\rho_g} = -K_v\nabla P_c \tag{20}$$

The apparent vapor diffusion coefficient $D_{va,mat}$, contains the impact of porous media. It is related to the binary diffusion coefficient in free space through porous media factor β. It can be simply written as $D^* = \beta D \cong \phi^{\frac{4}{3}} D$ (Diersch, 2006), where ϕ is the porosity of the fruit tissue (≅0.3 for fresh apple (Feng et al., 2004; Singh et al., 2015)), and D (≅2.42 × 10^{-5} m^2 s^{-1} (Prawiranto et al., 2018)) is the water diffusivity of intercellular air space.

Based on the above formulation, the natural diffusion flux (J_v) equals 0.3 μg s^{-1} m^{-2} for our specific case study. The quantified values for the average Coulomb force and the EHD-related mass flux inside the material are shown in Fig. 5. The fluxes generated due to the electric forces are in the order of 10^{-19} μg s^{-1} m^{-2}; therefore, they are negligible compared to the natural diffusion flux (i.e., when there is no electric field). The Coulomb force inside the material is too small due to the very small amount of free ions inside the material. Low space charge density results in a low Coulomb force-related mass flux inside the material.

3.5. *Electrocapillary flow inside the material*

This section will investigate the effect of the electric field on possible capillary water inside the pores of the food material. The amount of capillary water present inside the intercellular spaces, i.e., pores, of a fresh plant-based food material is limited compared to the water present inside the cells (Prawiranto et al., 2019). Nevertheless, several pretreatments induce cell membrane rupture to speed up the drying process. In these cases, a non-negligible amount of liquid water is present inside pores for food material with such damaged cells. In such conditions, the capillary water movement becomes an important transport process. Water movement is induced by capillary flow, which is influenced by the electrocapillary effect. In EHDD, electrocapillary action implies modifying the interfacial tension between the fruit cell wall and the water due to the presence of electrical charges (Chakraborty, 2014).

3.5.1. *Driving forces or resistances*

The unbalanced pressure within the air and water phases –i.e., two ends of the droplet in a capillary– is the driving force for water movement within a capillary. This pressure difference (ΔP_c) includes contributions from induced surface tension ($\Delta P_s = \frac{G\,\Delta\gamma_{LV}\cos(\theta)}{d_{pore}}$), gravity ($\Delta P_g = \rho_w g \Delta h$), and any external pressure source (ΔP_e) (Glockner and Naterer, 2006):

$$\Delta P_c = \Delta P_s + \Delta P_g + \Delta P_e \tag{21}$$

Here, d_{pore} is the pore diameter, G is a constant specific to pore geometry ($G = 4$ for circular pores), θ is the water contact angle on the food surface, and h is the water height inside the pore. We neglected the gravity and external pressures as the drying process is slow. With this assumption, ΔP_s is the only driving force that can be induced by electrocapillary or thermocapillary effects ($\Delta P_s = \Delta P_{s,ec} + \Delta P_{s,tc}$). Electrocapillary pressure ($P_{s,ec}$) is addressed in this section, and thermocapillary pressure ($P_{s,tc}$) will be discussed in the next section. In electrocapillary, applying an electric field will change the capillary pressure by changing the interfacial tension balance at the air–cell–water interface, hence changing the contact angle (Chakraborty, 2014).

3.5.2. *Quantifying the impact on the drying rate*

In this part, we quantify the magnitude of the electrocapillary pressure ($\Delta P_{s,ec}$) during EHD drying. Thereby, a liquid meniscus within a simple cylindrical pore with a radius of r_{pore} is considered. Chakraborty (2014) did an analytical calculation and defined equivalent electrocapillary pressure (P_{ec}) as:

$$\Delta P_{s,ec} = \frac{G\,\Delta\gamma_{ec}\cos(\theta)}{d_{pore}} = \frac{1}{2}\varepsilon_m\frac{\varphi_{SL}^2}{r_{pore}^2} \tag{22}$$

where, r_{pore} is the pore radius in plant-based foods (2–150 μm (Rahman et al., 2005)), and A_c is the cross-sectional area. In this equation, the equivalent charge-induced interfacial tension is $\Delta\gamma_{ec} = \varepsilon_m\frac{\varphi_{SL}^2}{\cos(\theta)\,r_{pore}\,G}$. Using Eq. (1), the water flux due to electrocapillary- induced pressure (J_{ec}) can be written as (Liu et al., 2018):

$$J_{ec} = -\frac{k_w}{\mu_w}\rho_w\nabla P_{s,ec} \tag{23}$$

where μ_w [kg m^{-1} s^{-1}] is the dynamic viscosity of water (1.002 × 10^{-3} kg m^{-1} s^{-1} at 20 °C), and $k_w \cong 10^{-13}$ m^2 (Feng et al.,

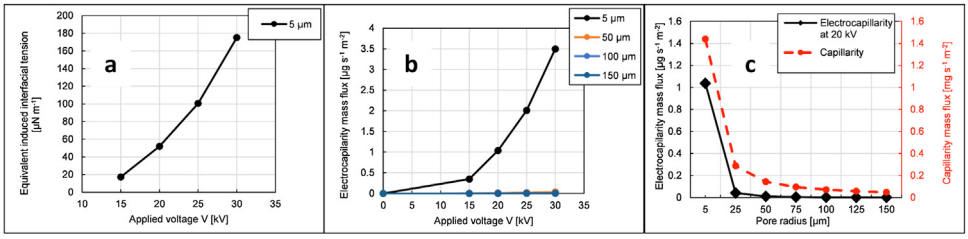

Fig. 6 – Quantified values for the electrocapillary flow inside the material; (a) equivalent induced interfacial tension due to presence of electric fields, (b) mass fluxes in different pore radii due to electrocapillarity vs. different applied voltages at the emitter electrode, (c) mass fluxes due to pure capillarity and electrocapillarity in a specific applied voltage at the emitter (20 kV) vs. different pore sizes. (For interpretation of the references to colour in the text, the reader is referred to the web version of this article.).

2004) is the water permeability. We quantified the water flux for the typical pore radii of plant-based foods (5–150 μm) and the typical values of applied voltages at the emitter in EHDD (15–30 kV). These voltages induce an electric field within the fruit of about 200–650 V cm^{-1}. The results are shown in Fig. 6. Note that the surface tension of water on fruit tissue is typically about 72.1 × 10^{-3} [N m^{-1}] (Sapper et al., 2019). Based on the results presented in Fig. 6a, the induced surface tension by electrocapillarity (max. 180 × 10^{-6} N m^{-1}) is several orders of magnitude smaller than the surface tension of water on fruit tissue (72.1 × 10^{-3} N m^{-1}). Therefore, the impact of the electrocapillarity (Fig. 6c in black color) is negligible compared to the natural capillarity during EHDD. The flux due to the pure capillary force (zero voltage) is also calculated and plotted for comparison (Fig. 6c in red color). As expected, electrocapillarity and pure capillarity fluxes are higher in the capillaries with lower diameters (Fig. 6b and c). Increasing the voltage increases the electrocapillarity flux in 5 μm capillaries significantly. This is very important because the density of pores with a radius less than 5 μm is higher than other sizes inside a fruit tissue (Rahman et al., 2005). Moreover, Fig. 6c shows that the electrocapillary-induced fluxes are not significant during EHDD compared to the natural capillarity fluxes (10^3 orders of magnitude difference).

3.6. *Thermocapillary flow at the material–air interface and inside the material*

In this section, we estimate the effect of the temperature gradient due to the electric field on the water at the material–air interface and inside the food material. Temperature gradient results in interfacial tension gradient along the liquid–air interface (Schönfeld, 2008). Such temperature gradients can occur due to differential evaporation at the air–liquid interface or non-homogeneous conduction inside the material. If electric fields are present, the conduction of electric current in a conductive medium due to the presence of high electrical fields results in volumetric heating called Joule or ohmic heating (Granot and Rubinsky, 2008). The Joule heating causes the spatial variation of surface tension and induces thermocapillary stresses to the liquid–air interface. In turn, thermocapillary stresses induce a spontaneous flow of a liquid film to a cooler position (Schönfeld, 2008). We refer to this heat-induced, pressure-driven flow as thermocapillary flow. Changing the liquid–solid contact angle and modifying the capillary flow are the other possible results of thermocapillary stresses. These effects can happen in surface water at the material–air interface as well as inside the material at intercellular pores and membrane nanopores (Dommersnes et al., 2005).

3.6.1. *Driving forces or resistances*

By considering Eq. (21) and the assumptions made in the previous section, the pressure difference between the drop ends due to the thermally induced surface tension differences is the driving force of the thermocapillary action. In EHDD, the electrical fields inside the material generate volumetric Joule heating and cause temperature gradients in the medium and possibly also at the surface (Granot and Rubinsky, 2008). Fluid flow due to the thermocapillary (or Marangoni effect) occurs because the surface tension at the cooler position is higher and induces a tangential force that moves the liquid droplet to the cooler place (Schönfeld, 2008). In other words, unbalanced surface energy results in a surface flow from lower interfacial tension areas (high temperature) towards higher interfacial tension (low temperature).

3.6.2. *Quantifying the impact on the drying rate*

Based on the literature, the temperature gradient at the material–air interface is negligible in EHDD (Singh et al., 2012; Bajgai et al., 2006). Moreover, for low-temperature gradients, the variation of droplet contact angle with temperature is very low ($\frac{\Delta\theta}{\Delta T} \cong -0.03$ to -0.1 [K^{-1}] (Bernardin et al., 1997)). According to Eqs. (14) and (15), for such a low variation of contact angle, the thermally-driven mass fluxes (Marangoni flow) at the material–air interface are negligible. For the thermocapillary effect inside the material, Raso and Heinz (2006) investigated the local temperature rise due to the Joule effect in different elements of food material. They proved that the ratio of the temperature rise in a membrane surface to the surrounding media is equal to $\frac{\sigma_c}{\sigma_m} \sim 10^5$ which is higher than other element in a food material. Therefore, we quantify the Joule heating and thermocapillary effects at the membrane because it is more likely to happen there. σ_c and σ_m are mean specific electrical conductivities of the medium and membrane, respectively [Ω^{-1} m^{-1}].

The temperature rise due to Joule heating during EHDD is proportional to the time t and the current density through the media $j = \sigma_c E$. By taking into account the impact of heat diffusion through the membrane ($\sqrt{\chi t}/d_m$), the Joule heating effect can be written as follows (Raso and Heinz, 2006):

$$\Delta T_J = \frac{j^2 t^{0.5} d_m}{\chi^{0.5} \sigma_m \rho_w C} \tag{24}$$

where t is the time [s] of applying the electric field, j is current density [A m^{-1}], χ is thermal diffusivity [m^2 s^{-1}], d_m is the membrane width, and C specific heat capacity of the

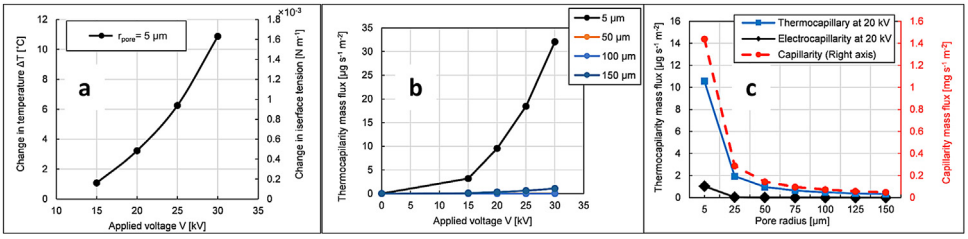

Fig. 7 – Quantified values for the thermocapillary flow inside the material; (a) temperature rise and associated change of surface tension vs. different applied voltages at the emitter electrode for a capillary with 5 μm radius, (b) mass fluxes in different pore radii due to thermocapillary vs. different applied voltages at the emitter electrode, (c) mass fluxes due to pure capillarity and thermocapillary, and electrocapillarity in a specific applied voltage at the emitter (20 kV) vs. different pore sizes.

medium [J kg^{-1} K^{-1}]. According to (Glockner and Naterer, 2006) water surface tension varies with temperature as $\gamma = 10^{-3}(75.83 - 0.1477T)$ and hence $\Delta\gamma_{th} = -10^{-3}(0.1477\Delta T)$. In order to use this time-dependent variable in our steady state equations we have to consider the steady-state temperature rise. Details and the graphs of the obtained values under steady-state conditions are available in Section 5 of the supplementary material. The equivalent thermocapillary pressure inside pores due to surface tension variation is:

$$\Delta P_{s,th} = \frac{G\,\Delta\gamma_{th}\cos(\theta)}{d_{pore}} \tag{25}$$

Thermocapillary flux can be written as follows:

$$J_{th} = -\frac{k_w}{\mu_w}\rho_w \nabla P_{s,th} \tag{26}$$

The results are presented in Fig. 7. In Fig. 7a, the temperature rise due to the Joule heating is shown for a capillary with 5 μm radius. The temperature rise can amount to 10 °C, which results in a change of the surface tension up to 1.6 mN m^{-1} (Fig. 7a). The mass flux due to the thermocapillary flow in capillary exponentially increases by increasing the applied voltage at the emitter (Fig. 7b). Like all the other sources of capillarity, the thermocapillary impact is higher in smaller pores. The fluxes due to the thermocapillary, electrocapillary, and natural capillarity action (zero voltage) are presented in Fig. 7c. The thermocapillary-induced fluxes are larger than electrocapillary fluxes, but both of them are several orders of magnitude smaller than the natural capillarity fluxes. Therefore, the electric field-induced capillary flow contribution is negligible compared to the natural capillarity during EHDD.

3.7. *Electro-osmotic flow*

In this section, we quantify how electro-osmosis in porous materials like fruits during EHDD can contribute to the water transport process. Besides EFDF, which was discussed in Section 3.4, the presence of electric charges on the cell membrane, the pores, and capillary surfaces inside the fruit tissue affects the ion distribution of the liquid and forms the electrical double layer (EDL) (Li, 2004). EDL consists of a compact layer of immobile balanced charges and a diffuse layer of mobile ions (Fig. 8). In the diffuse layer, the density of the counter ions –positive ions in Fig. 8– is higher. The presence of an external electric field induces an electrical force to the excess counter-ions in the diffuse layer and causes the fluid to flow. This phenomenon is called electro-osmosis, and the resulting flow is called electro-osmotic flow (EOF).

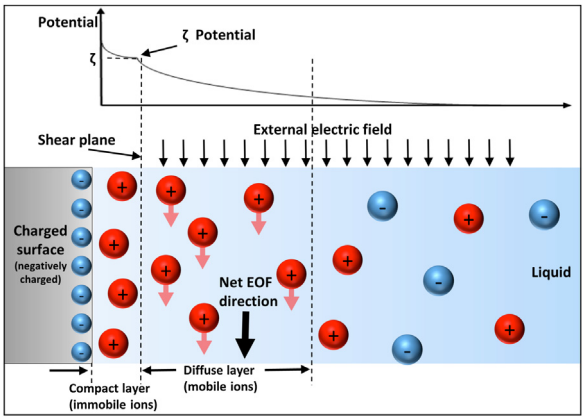

Fig. 8 – Illustration of the potential field and the ionic concentration field in an electrical double layer for a flat surface in contact with an aqueous solution. The external electric field moves the ions inside the media and causes a net flow called EOF.

3.7.1. *Driving forces or resistances*

The pressure gradient induced by the applied electric field is the main driving force in EOF. The water inside the material and the cell cytoplasm are conductive mediums surrounded by a membrane or capillary surfaces with dielectric characteristics. According to the Lippmann theory, by increasing the applied electric field between a conductive liquid (i.e., droplet or film) and a solid surface, EDL's net charge density increases. This leads to an increase in the electric forces acting on the ions in the liquid (Xu et al., 2021).

3.7.2. *Quantifying the impact on the drying rate*

Because the Reynolds number inside the material is extremely small, we consider the water as an incompressible fluid under steady-state conditions. The velocity u_{EOF} due to the electro-osmosis flow is considered as the velocity vector. The electro-osmosis velocity u_{EOF} for a single pore is defined by considering the balance between viscous and electrical forces (Di Fraia et al., 2018; Maier et al., 2016):

$$u_E = \frac{\varepsilon_0 \varepsilon_m \zeta}{\mu_w} E \tag{27}$$

where ζ [V] is the zeta potential at the wall (see Fig. 8), the water flux can be written as follow:

$$J_{EOF} = J_l = -\frac{k_w}{\mu_w}\rho_w \nabla(P_c) = -\rho_w u_E \tag{28}$$

We calculated EOF for a single pore under various applied voltages at the emitter using the above formula (Fig. 9). The

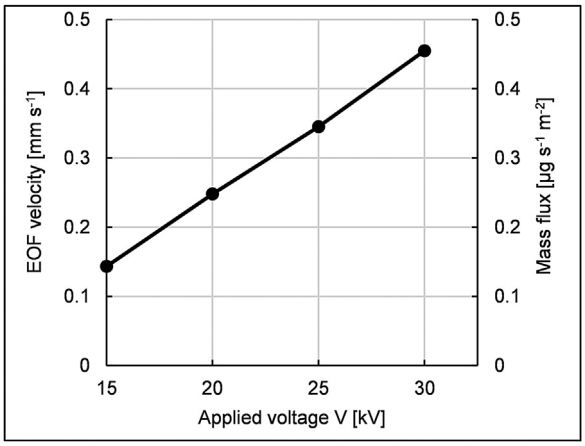

Fig. 9 – Quantified values for the electro-osmotic flow (EOF) inside a single pore with respect to the applied voltages at the emitter electrode.

mass flux and EOF velocity linearly increase with increasing the voltage. It implies that for a higher EOF flux, hence a better drying rate, operating with higher voltages could be beneficial.

3.8. *Membrane electroporation and transmembrane flow*

In this section, we quantify how an electric field over cellular materials like fruits during EHDD can change the cell membrane permeability. Electric modification of cell membrane permeability or so-called electroporation is defined as an increase in the number and/or size of the hydrophilic nanopores (i.e., aqueous pathways) in cellular membranes. It is due to an elevated electric potential difference between the membrane's inner and outer surfaces caused by the external electric field. It results in higher membrane permeability and, consequently, higher transmembrane water transport for two reasons. First, the additional and larger nanopores facilitate molecular transport across the cell membranes by increasing the hydrodynamic permeability of the membranes. Second, electrokinetic effects (electro-osmosis, electrophoresis) induced by the transmembrane electric potential affect the molecular transport (Smith and Weaver, 2011). Membrane electroporation has different applications, especially in plant tissue treatment via the pulsed electric field (PEF) method and introducing gene material into living cells (Zhang, 1991).

3.8.1. *Driving forces or resistances*

The applied external electric field is the driving force of membrane electroporation which results in decreasing the resistance against water flux across the cell membrane. The cell membrane has dielectric properties, and there is an electric potential difference between the inner and outer sides of the membrane (Tosteson, 1989). It can be considered as a capacitor with two plates and a dielectric in between. Applying an external electric field increases this potential difference and induces higher electrical stress on the membrane (Zhang, 1991). By increasing the electric field strength, the pores increase in size and number until the membrane ruptures (dielectric breakdown) at the critical transmembrane voltage, $U_{m,crit}$ (Zhang, 1991; Chen et al., 2006; Movahed and Li, 2012).

3.8.2. *Quantifying the impact on the drying rate*

We assumed that the number of pores at the membrane determines the cell membrane permeability. Accordingly, we considered that the initial cell permeability (at zero voltage) is equivalent to a pore density of N_0 [cm^{-2}]. In this regard, using the formulation provided in (Kanani et al., 2010) for the initial membrane water permeability ($K_m^0 = 7.4 \times 10^{-19}$ [s]), the equivalent pore density N_0 is 15×10^4 [cm^{-2}]. (Granot and Rubinsky (2008)) employed the Krassowska model to calculate N as follows:

$$N = N_0 e^{q\left(\frac{\bar{U}_m}{U_{m,th}}\right)^2} \tag{29}$$

In this equation, $q = 2.46$ is the electroporation constant, $e \cong 2.71$ is the Euler's or so-called Napier's number, $\bar{U}_m$ [V] is the average transmembrane potential difference across the membrane, and $U_{m,th}$ is the threshold strength (typically 0.2–1 V) that the electrical stresses lead to the appearance of local defects (pores) at the membrane surface (Chen et al., 2006). Details about the calculation of $\bar{U}_m$ are available in the Supplementary material. Variation of the membrane water permeability $\frac{k_m}{k_m^0}$ is proportional to the variation of the membrane porosity, which in turn is proportional to the variation of the pore density $\frac{N}{N_0}$ (Kanani et al., 2010). Therefore:

$$k_m = \frac{N}{N_0} k_m^0 \tag{30}$$

The water flux through the cell membrane J_m is defined as (Prawiranto et al., 2018; Granot and Rubinsky, 2008):

$$J_m = J_l = -\frac{k_l}{\mu_l}\rho_l \nabla (P_c) = -\frac{k_m}{L_m}(\psi_c - \psi_w) \tag{31}$$

where ψ_w and ψ_c are the water potential at the cell wall (outside of the membrane) and protoplast (inside of the membrane), respectively. Details about the calculation of ψ_w and ψ_c are available in the Supplementary material. L_m is membrane thickness (≈10 nm).

The results are represented in Fig. 10. Increasing the voltage always results in higher electroporation and higher mass flux (Fig. 10). Regarding time, membrane permeability changes up to 90 min, but after 90 min, there is no change in the permeability for any applied voltage. It can be concluded that regardless of the voltage, pore formation will be saturated in 90 min. We used the obtained permeabilities after 90 min for our steady-state flux equations. Note that for voltages above 25 kV, the pore formation starts immediately after starting the process, but it takes time at lower voltages. At very high voltages such as 30 kV, the largest change in permeability occurs during the first few minutes (Fig. 10a). It implies that for having a better drying rate, one of the strategies could be starting the drying process at very high voltages for a few minutes and continuing the process at lower voltages to save energy.

4. Ranking the transport mechanisms based on their contribution

In the above sections, based on previous works and literature, we considered all possible water transport mechanisms that could take place during EHDD. The results are presented based on mass flux. To compare the relative contribution of each transport mechanism for our specific case study, the steady-state fluxes and flow rates for a capillary with 5 μm radius are calculated. The selected pore radius has the highest contribution in the pore-size distribution of plant-based food (Rahman

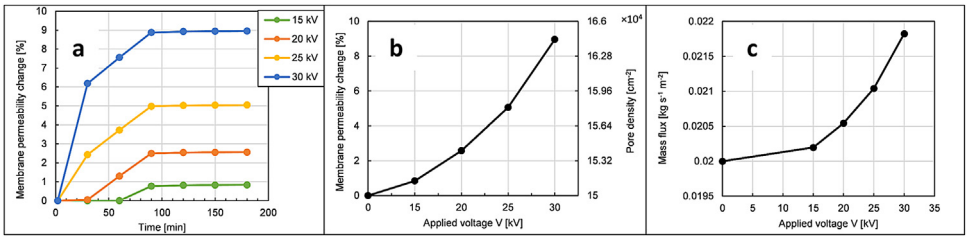

Fig. 10 – Quantified values for membrane electroporation and the transmembrane flow inside the material; (a) variation of membrane permeability pore density vs. time for different applied voltages at the emitter electrode, (b) pore density and percentage of change in membrane permeability for different applied voltages at the emitter electrode, (c) transmembrane water flux for different applied voltages at the emitter electrode.

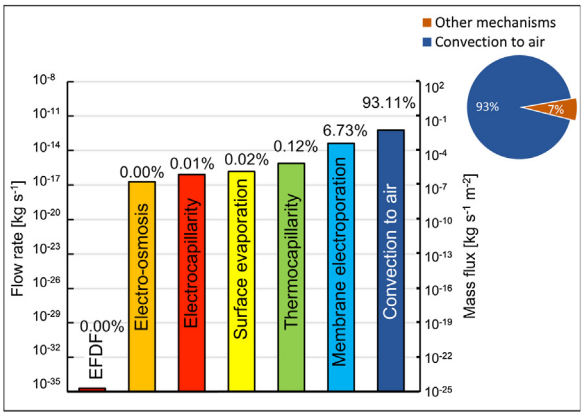

Fig. 11 – Contribution of different EHD-induced water transport mechanisms to the total mass transfer during the EHD drying process.

et al., 2005). Fig. 11 shows the contribution of each transport mechanism in the total mass transfer. Note that the presented results in the figure are the changes induced by EHD. Fluxes due to the natural dehydration mechanisms such as natural convection and capillarity are not included. They are considered as the benchmark. Convection to air due to the ionic wind is the dominant mechanism. Therefore, this study verifies that EHD drying is a convective-based process, as stated in previous studies. Membrane electroporation is the second important mechanism that contributes to the total mass transfer rate. As can be seen in the figure, the contributions of the other mechanisms are not significant.

5. Discussion

This study hints at the driving forces that should be focused on for EHD drying to further improve the drying rate when using this technology. For instance, the importance of the airflow to effectively distribute the airflow around the sample is now obvious. It improves the total drying rate by increasing the evaporation mechanisms. As discussed, operating in higher voltages at the beginning of the drying process increases the transmembrane flow, hence the total drying rate, while keeping the process energy-efficient. Moreover, AC voltage with low frequency instead of pure DC can provoke membrane electroporation. Another advantage of using AC voltage with low frequency, which was not explored in this study, is avoiding the accumulation of charges on the drying material surface. Because while operating the EHD dryer for a long time in DC mode, free charges will be deposited at the dielectric surfaces, such as the drying material surface (Blennow et al., 2000). Consequently, this electrostatic induction leads to a counteracting electric field component, which reduces the total electric field in the domain between the emitter and the collector (Blennow et al., 2000). Changing the polarity of the applied voltage from time to time (i.e., AC voltage with a low frequency) can reduce this undesirable phenomenon. The AC frequency should be low in the range from 10 to 100 Hz to avoid temperature rise in the drying material due to Joule heating.

Another possibility is further destabilization of the boundary layer (and consequently increase the convection and evaporation mechanisms) by modulating carrier frequency with the patches of higher frequency in the range of kHz. It can increase the turbulence level of the generated ionic wind and enhance the ability of the airflow to remove the moisture from the material boundary layer. This technique has been widely used in aerodynamics to destabilize the boundary layer (see Iranshahi and Mani (2018), Benard and Moreau (2012), Corke and Post (2005)). It may have another advantage of membrane excitation and increasing the electroporation without significant enhancement of the local temperature (important for heat-sensitive components in food).

It should be noted that the calculations are performed for the constant drying rate period where the resistance to mass transfer by external factors such as convection is much greater than the internal resistances like capillary action or membrane permeability (Plumb, 2000). As we showed, the electric field's impact is mostly on the internal resistances. Therefore, the EHD-driven mass transport mechanisms could be of higher importance in the subsequent decreasing drying rate period where the mass transfer is internally controlled. As such, we predict that the drying rate difference between the EHDD and pure convective dehydration during falling rate periods is higher.

6. Conclusion

The contribution of different water transport mechanisms during EHD drying of plant-based foods is investigated. The mass fluxes and drying rates of the identified mechanisms are estimated at the constant drying rate period and ranked based on their contribution to the total drying rate. It is shown that convection to the air is the dominant mechanism in EHD drying. Moreover, cell membrane electroporation has a considerable contribution to the total mass transfer. The contribution of the other driving forces and mechanisms, such as electro-osmosis and thermocapillary flow, is not significant. The reported difference in the drying rate between the convective drying and EHD drying is caused by these additional dehydration mechanisms, which are activated due to the electric field's presence. This study can be considered as the next step towards establishing a full physics-based

model of the dehydration process, including the falling rate period. Moreover, the results of this paper can be helpful to further understand the EHD drying process towards performance improvement and industrial implementation of this promising technology.

Author contributions

K. Iranshahi and T. Defraeye conceptualized the study. T. Defraeye did project administration, wrote the project proposal, and secured the funding; K. Iranshahi and T. Defraeye developed the methodology; K. Iranshahi performed the theoretical modeling and calculations; K. Iranshahi performed analysis and interpretation of the results; T. Defraeye performed supervision of K. Iranshahi. K. Iranshahi wrote the original draft with key input from T. Defraeye and D. Onwude; D. Onwude, T. Defraeye and A. Martynenko critically reviewed and edited the manuscript, and K. Iranshahi revised the manuscript on the basis of these suggestions.

Declaration of interests

The authors declare that they have no known competing financial interests or personal relationships that could have appeared to influence the work reported in this paper.

Declaration of Competing Interest

The authors report no declarations of interest.

Acknowledgments

The authors acknowledge the ETH Foundation and the World Food System Center of ETH Zurich for supporting this project.

Appendix A. Supplementary data

Supplementary material related to this article can be found, in the online version, at doi:https://doi.org/10.1016/j.fbp.2021.11.009.

References

Alem-Rajabif, A., Lai, F.C., 2005. EHD-enhanced drying of partially wetted glass beads. Dry. Technol. 23 (March (3)), 597–609, http://dx.doi.org/10.1081/DRT-200054150.

Aregawi, W.A., Abera, M.K., Fanta, S.W., Verboven, P., Nicolai, B., 2014. Prediction of water loss and viscoelastic deformation of apple tissue using a multiscale model. J. Phys. Condens. Matter 26 (November (46)), 464111, http://dx.doi.org/10.1088/0953-8984/26/46/464111.

Bajgai, T.R., Raghavan, G.S.V., Hashinaga, F., Ngadi, M.O., 2006. Electrohydrodynamic drying — a concise overview. Dry. Technol. 24 (7), 905–910, http://dx.doi.org/10.1080/07373930600734091.

Bardy, E., Hamdi, M., Havet, M., Rouaud, O., 2015. Transient exergetic efficiency and moisture loss analysis of forced convection drying with and without electrohydrodynamic enhancement. Energy 89 (September), 519–527, http://dx.doi.org/10.1016/j.energy.2015.06.017.

Benard, N., Moreau, E., 2012. EHD force and electric wind produced by plasma actuators used for airflow control. 6th AIAA Flow Control Conference, 1–47, http://dx.doi.org/10.2514/6.2012-3136, no. June.

Bernardin, J.D., Mudawar, I., Walsh, C.B., Franses, E.I., 1997. Contact angle temperature dependence for water droplets on practical aluminum surfaces. Int. J. Heat Mass Transf. 40 (March (5)), 1017–1033, http://dx.doi.org/10.1016/0017-9310(96)00184-6.

Blennow, H.J.M., Sjoberg, M.L.-A., Leijon, M.A.S., Gubanski, S.M., 2000. Electric field reduction due to charge accumulation in a dielectric-covered electrode system. IEEE Trans. Dielectr. Electr. Insul. 7 (June (3)), 340–345, http://dx.doi.org/10.1109/94.848912.

Cengel, Y., 2014. Mass transfer. In: Heat and Mass Transfer: Fundamentals and Applications. McGraw-Hill Higher Education, pp. 717–785.

Chakraborty, S., 2014. Electrocapillary. In: Encyclopedia of Microfluidics and Nanofluidics. Springer US, Boston, MA, pp. 1–15.

Chen, C., Smye, S.W., Robinson, M.P., Evans, J.A., 2006. Membrane electroporation theories: a review. Med. Biol. Eng. Comput. 44 (March (1–2)), 5–14, http://dx.doi.org/10.1007/s11517-005-0020-2.

Choi, W.Y., Park, H.J., Ahn, D.J., Lee, J., Lee, C.Y., 2002. Wettability of chitosan coating solution on'Fuji' apple skin. J. Food Sci. 67 (September (7)), 2668–2672, http://dx.doi.org/10.1111/j.1365-2621.2002.tb08796.x.

Corke, T., Post, M., 2005. Overview of plasma flow control: concepts, optimization, and applications. 43rd AIAA Aerospace Sciences Meeting and Exhibit, 13205–13219, http://dx.doi.org/10.2514/6.2005-563, no. January.

Datta, A.K., 2007. Porous media approaches to studying simultaneous heat and mass transfer in food processes. I: problem formulations. J. Food Eng. 80 (May (1)), 80–95, http://dx.doi.org/10.1016/j.jfoodeng.2006.05.013.

Defraeye, T., Martynenko, A., 2018a. Electrohydrodynamic drying of food: new insights from conjugate modeling. J. Clean. Prod. 198, 269–284, http://dx.doi.org/10.1016/j.jclepro.2018.06.250.

Defraeye, T., Martynenko, A., 2018b. Future perspectives for electrohydrodynamic drying of biomaterials. Dry. Technol. 36 (January (1)), 1–10, http://dx.doi.org/10.1080/07373937.2017.1326130.

Defraeye, T., Martynenko, A., 2019. Electrohydrodynamic drying of multiple food products: evaluating the potential of emitter-collector electrode configurations for upscaling. J. Food Eng. 240 (July), 38–42, http://dx.doi.org/10.1016/j.jfoodeng.2018.07.011, 2018.

Defraeye, T., Verboven, P., 2017. Convective drying of fruit: role and impact of moisture transport properties in modelling. J. Food Eng. 193 (January), 95–107, http://dx.doi.org/10.1016/j.jfoodeng.2016.08.013.

Di Fraia, S., Massarotti, N., Nithiarasu, P., 2018. Modelling electro-osmotic flow in porous media: a review. Int. J. Numer. Methods Heat Fluid Flow 28 (February (2)), 472–497, http://dx.doi.org/10.1108/HFF-11-2016-0437.

Diersch, H.-J.G., 2006. Gas Transport in Porous Media, vol. 20. Springer Netherlands, Berlin, Heidelberg.

Digilov, R., 2000. Charge-induced modification of contact angle: the secondary electrocapillary effect. Langmuir 16 (August (16)), 6719–6723, http://dx.doi.org/10.1021/la991308a.

Dolati, F., Amanifard, N., Deylami, H.M., 2018. Numerical investigation of moisture removal and energy consumption of porous body affected by EHD. Energy 154, 352–364, http://dx.doi.org/10.1016/j.energy.2018.04.143.

Dommersnes, P.G., Orwar, O., Brochard-Wyart, F., Joanny, J.F., 2005. Marangoni transport in lipid nanotubes. Europhys. Lett. 70 (April (2)), 271–277, http://dx.doi.org/10.1209/epl/i2004-10477-9.

Feng, H., Tang, J., Plumb, O.A., Cavalieri, R.P., 2004. Intrinsic and relative permeability for flow of humid air in unsaturated apple tissues. J. Food Eng. 62 (April (2)), 185–192, http://dx.doi.org/10.1016/S0260-8774(03)00231-0.

Garai, J., 2009. Physical model for vaporization. Fluid Phase Equilib. 283 (September (1–2)), 89–92, http://dx.doi.org/10.1016/j.fluid.2009.06.005.

Glockner, P.S., Naterer, G.F., 2006. Surface tension and frictional resistance of thermocapillary pumping in a closed microchannel. Int. J. Heat Mass Transf. 49 (November (23–24)),

4424–4436, http://dx.doi.org/10.1016/j.ijheatmasstransfer.2006.05.005.
Goodenough, T.I.J., Goodenough, P.W., Goodenough, S.M., 2007. The efficiency of corona wind drying and its application to the food industry. J. Food Eng. 80 (June (4)), 1233–1238, http://dx.doi.org/10.1016/j.jfoodeng.2006.09.016.
Granot, Y., Rubinsky, B., 2008. Mass transfer model for drug delivery in tissue cells with reversible electroporation. Int. J. Heat Mass Transf. 51 (November (23–24)), 5610–5616, http://dx.doi.org/10.1016/j.ijheatmasstransfer.2008.04.041.
Gunasekaran, S., 1999. Pulsed microwave-vacuum drying of food materials. Dry. Technol. 17 (3), 395–412, http://dx.doi.org/10.1080/07373939908917542.
Huang, X., Qi, T., Wang, Z., Yang, D., Liu, X., 2012. A moisture transmembrane transfer model for pore network simulation of plant materials drying. Dry. Technol. 30 (December (15)), 1742–1749, http://dx.doi.org/10.1080/07373937.2012.718306.
Iranshahi, K., Mani, M., 2018. Dielectric barrier discharge actuators employed as alternative to conventional high-lift devices. J. Aircr. 55 (September (5)), 1–10, http://dx.doi.org/10.2514/1.C034690.
Iranshahi, K., Martynenko, A., Defraeye, T., 2020. Cutting-down the energy consumption of electrohydrodynamic drying by optimizing mesh collector electrode. Energy 208, 118168.
Jeyamkondan, S., Jayas, D.S., Holley, R.A., 1999. Pulsed electric field processing of foods: a review. J. Food Prot. 62 (September (9)), 1088–1096, http://dx.doi.org/10.4315/0362-028X-62.9.1088.
Jiang, C., Ma, H., Hasko, D.G., Nathan, A., 2016. Influence of polarization on contact angle saturation during electrowetting. Appl. Phys. Lett. 109, 211601, http://dx.doi.org/10.1063/1.4968189.
Kanani, D.M., Fissell, W.H., Roy, S., Dubnisheva, A., Fleischman, A., Zydney, A.L., 2010. Permeability–selectivity analysis for ultrafiltration: effect of pore geometry. J. Membr. Sci. 349 (March (1–2)), 405–410, http://dx.doi.org/10.1016/j.memsci.2009.12.003.
Lai, F.C., Sharma, R.K., 2005. EHD-enhanced drying with multiple needle electrode. J. Electrostat. 63 (3–4), 223–237, http://dx.doi.org/10.1016/j.elstat.2004.10.004.
Leu, J.S., Jang, J.Y., Wu, Y.H., 2018. Optimization of the wire electrode height and pitch for 3-D electrohydrodynamic enhanced water evaporation. Int. J. Heat Mass Transf. 118 (March), 976–988, http://dx.doi.org/10.1016/j.ijheatmasstransfer.2017.11.056.
Li, D., 2004. Electroosmotic flows in microchannels. In: Li, Dongqing (Ed.), Electrokinetics in Microfluidics, vol. 2. Elsevier, pp. 92–203.
Lin, T.M., Durance, T.D., Scaman, C.H., 1998. Characterization of vacuum microwave, air and freeze dried carrot slices. Food Res. Int. 31 (March (2)), 111–117, http://dx.doi.org/10.1016/S0963-9969(98)00070-2.
Liu, M., Wu, J., Gan, Y., Hanaor, D.A.H., Chen, C.Q., 2018. Tuning capillary penetration in porous media: combining geometrical and evaporation effects. Int. J. Heat Mass Transf. 123 (August), 239–250, http://dx.doi.org/10.1016/j.ijheatmasstransfer.2018.02.101.
Maier, R.S., Nybo, E., Seymour, J.D., Codd, S.L., 2016. Electroosmotic flow and dispersion in open and closed porous media. Transp. Porous Media 113 (May (1)), 67–89, http://dx.doi.org/10.1007/s11242-016-0680-4.
Martynenko, A., Kudra, T., 2016. Electrohydrodynamic (EHD) drying of grape pomace. Japan J. Food Eng. 17 (4), 123–129, http://dx.doi.org/10.11301/jsfe.17.123.
Martynenko, A., Astatkie, T., Riaud, N., Wells, P., Kudra, T., 2017. Driving forces for mass transfer in electrohydrodynamic (EHD) drying. Innov. Food Sci. Emerg. Technol. 43 (May), 18–25, http://dx.doi.org/10.1016/j.ifset.2017.07.022.
Martynenko, A., Zheng, W., 2016. Electrohydrodynamic drying of apple slices: energy and quality aspects. J. Food Eng. 168 (January), 215–222, http://dx.doi.org/10.1016/j.jfoodeng.2015.07.043.
Monrolin, N., Praud, O., Plouraboué, F., 2018. Electrohydrodynamic ionic wind, force field, and ionic mobility in a positive dc wire-to-cylinders corona discharge in air. Phys. Rev. Fluids 3 (June (6)), 063701, http://dx.doi.org/10.1103/PhysRevFluids.3.063701.
Moreau, E., Touchard, G., 2008. Enhancing the mechanical efficiency of electric wind in corona discharges. J. Electrostat. 66 (January (1–2)), 39–44, http://dx.doi.org/10.1016/J.ELSTAT.2007.08.006.
Movahed, S., Li, D., 2012. Electrokinetic transport through the nanopores in cell membrane during electroporation. J. Colloid Interface Sci. 369 (March (1)), 442–452, http://dx.doi.org/10.1016/j.jcis.2011.12.039.
Mujumdar, A.S., Devahastin, S., 2000. Fundamental principles of drying. In: Mujumdar's Practical Guide to Industrial Drying. Exergex, Brossard, Canada, pp. 1–22.
Nikzad, M., Azimian, A.R., Rezaei, M., Nikzad, S., 2017. Water liquid-vapor interface subjected to various electric fields: a molecular dynamics study. J. Chem. Phys. 147 (November (20)), 204701, http://dx.doi.org/10.1063/1.4985875.
Peek, F.W., 1920. Dielectric Phenomena in High Voltage Engineering. McGraw-Hill Book Company, Incorporated.
Picknett, R.G., Bexon, R., 1977. The evaporation of sessile or pendant drops in still air. J. Colloid Interface Sci. 61 (September (2)), 336–350, http://dx.doi.org/10.1016/0021-9797(77)90396-4.
Plumb, O.A., 2000. Transport phenomena in porous media: modeling the drying process. In: Vafai, K. (Ed.), Handbook of Porous media. , 1st ed. CRC Press/Taylor & Francis, pp. 755–785.
Prawiranto, K., Defraeye, T., Derome, D., Verboven, P., Nicolai, B., Carmeliet, J., 2018. New insights into the apple fruit dehydration process at the cellular scale by 3D continuum modeling. J. Food Eng. 239 (December), 52–63, http://dx.doi.org/10.1016/j.jfoodeng.2018.06.023.
Prawiranto, K., et al., 2019. Impact of drying methods on the changes of fruit microstructure unveiled by X-ray micro-computed tomography. RSC Adv. 9 (April (19)), 10606–10624, http://dx.doi.org/10.1039/c9ra00648f.
Rahman, M.S., Al-Zakwani, I., Guizani, N., 2005. Pore formation in apple during air-drying as a function of temperature: porosity and pore-size distribution. J. Sci. Food Agric. 85 (April (6)), 979–989, http://dx.doi.org/10.1002/jsfa.2056.
Ramírez, C., Gallegos, I., Ihl, M., Bifani, V., 2012. Study of contact angle, wettability and water vapor permeability in carboxymethylcellulose (CMC) based film with murta leaves (Ugni molinae Turcz) extract. J. Food Eng. 109 (April (3)), 424–429, http://dx.doi.org/10.1016/j.jfoodeng.2011.11.005.
Raso, J., Heinz, V., 2006. Pulsed Electric Fields Technology for the Food Industry. Springer US, Boston, MA.
Robinson, M., 1961. Movement of air in the electric wind of the corona discharge. Trans. Am. Inst. Electr. Eng. I Commun. Electron. 80 (July (2)), 143–150, http://dx.doi.org/10.1109/TCE.1961.6373091.
Sapper, M., Bonet, M., Chiralt, A., 2019. Wettability of starch-gellan coatings on fruits, as affected by the incorporation of essential oil and/or surfactants. LWT 116 (December), 108574, http://dx.doi.org/10.1016/j.lwt.2019.108574.
Schönfeld, F., 2008. Droplet evaporation. In: Encyclopedia of Microfluidics and Nanofluidics. Springer US, Boston, MA, pp. 418–423.
Semenov, S., Starov, V.M., Rubio, R.G., Agogo, H., Velarde, M.G., 2011. Evaporation of sessile water droplets: universal behaviour in presence of contact angle hysteresis. Colloids Surfaces A Physicochem. Eng. Asp. 391 (November (1–3)), 135–144, http://dx.doi.org/10.1016/j.colsurfa.2011.07.013.
Shrimpton, J., 2009. Charge Injection Systems. Springer Berlin Heidelberg, Berlin, Heidelberg.
Singh, A., Orsat, V., Raghavan, V., 2012. A comprehensive review on electrohydrodynamic drying and high-voltage electric field in the context of food and bioprocessing. Dry. Technol. 30 (December (16)), 1812–1820, http://dx.doi.org/10.1080/07373937.2012.708912.
Singh, F., Katiyar, V.K., Singh, B.P., 2015. Mathematical modeling to study influence of porosity on apple and potato during

dehydration. J. Food Sci. Technol. 52 (September (9)), 5442–5455, http://dx.doi.org/10.1007/s13197-014-1647-5.
Smith, K.C., Weaver, J.C., 2011. Transmembrane molecular transport during versus after extremely large, nanosecond electric pulses. Biochem. Biophys. Res. Commun. 412 (August (1)), 8–12, http://dx.doi.org/10.1016/j.bbrc.2011.06.171.
Srikiatden, J., Roberts, J.S., 2007. Moisture transfer in solid food materials: a review of mechanisms, models, and measurements. Int. J. Food Prop. 10 (October (4)), 739–777, http://dx.doi.org/10.1080/10942910601161672.
Sumariyah, Khuriati, A., Fachriyah, E., 2018. Ion wind generation and its application to drying of wild Ginger slices (*Curcuma Xanthorhiza*). J. Phys. Conf. Ser. 1025 (May (1)), http://dx.doi.org/10.1088/1742-6596/1025/1/012016.
Tosteson, D.C. (Ed.), 1989. Membrane Transport. Springer New York, New York, NY.
Vancauwenberghe, V., Di Marco, P., Brutin, D., 2013. Wetting and evaporation of a sessile drop under an external electrical field: a review. Colloids Surf. A Physicochem. Eng. Asp. 432 (September), 50–56, http://dx.doi.org/10.1016/j.colsurfa.2013.04.067.
Velev, O.D., Bhatt, K.H., 2006. On-chip micromanipulation and assembly of colloidal particles by electric fields. Soft Matter 2 (9), 738, http://dx.doi.org/10.1039/b605052b.
Washizu, M., Suzuki, S., Kurosawa, O., Nishizaka, T., Shinohara, T., 1994. Molecular dielectrophoresis of biopolymers. IEEE Trans. Ind. Appl. 30 (4), 835–843, http://dx.doi.org/10.1109/28.297897.
Whitaker, S., 1977. Simultaneous heat, mass, and momentum transfer in porous media: a theory of drying. Adv. Heat Transf. 13 (January (C)), 119–203, http://dx.doi.org/10.1016/S0065-2717(08)70223-5.
Xu, W., Song, Y., Xu, R.X., Wang, Z., 2021. Electrohydrodynamic and hydroelectric effects at the water–solid interface: from fundamentals to applications. Adv. Mater. Interfaces 8 (January (2)), 2000670, http://dx.doi.org/10.1002/admi.202000670.
Zang, D., Tarafdar, S., Tarasevich, Y.Y., Dutta Choudhury, M., Dutta, T., 2019. Evaporation of a droplet: from physics to applications. Phys. Rep. 804 (April), 1–56, http://dx.doi.org/10.1016/j.physrep.2019.01.008, Elsevier B.V.
Zhang, L., 1991. Electroporation and electrofusion in cell biology. Bioelectrochem. Bioenerg. 26 (October (2)), 376–377, http://dx.doi.org/10.1016/0302-4598(91)80050-D.
Zhang, M., Chen, H., Mujumdar, A.S., Zhong, Q., Sun, J., 2015. Recent developments in high-quality drying with energy-saving characteristic for fresh foods. Dry. Technol. 33 (October (13)), 1590–1600, http://dx.doi.org/10.1080/07373937.2015.1012267.